

**1 Wind Veer and Speed in Turbulent Ekman Flow Part I:  
2 Scaling analysis and universal profile model**

**3 Cedrick Ansorge<sup>1</sup> and Hauke Wurps<sup>2,3</sup>**

**4**  
**5** Submitted October 31, 2024

**6 Abstract**

**7** The profiles of wind speed and direction in turbulent Ekman flow are formulated  
**8** based on asymptotic theory and data from direct numerical simulation. The profile  
**9** of the streamwise component follows the classical viscous, logarithmic and wake  
**10** scaling. In the outer layer, the velocity component profiles can be described by an  
**11** Ekman-spiral with adapted boundary conditions that result in a reduction of the  
**12** spiral-like rotation. The span-wise component poses a conceptual challenge to the  
**13** channel-flow analogy in the context of asymptotic matching; it exhibits a mixed  
**14** scaling in the surface layer, but follows outer scaling for most of the outer layer.  
**15** Viscous stress scales universally across the boundary layer in inner units while  
**16** the total stress becomes universal as a function of outer height. This implies a  
**17** mixed scaling for the turbulent stress and eddy viscosity across the inner layer  
**18** and convergence to a universal scaling as function of the outer height across the  
**19** outer layer for increasing scale separation vide Reynolds numbers.

**20 1 Introduction**

**21** The Coriolis force bends the path of motion on a rotating sphere and establishes  
**22** geostrophic equilibrium when in balance with a pressure gradient force. Wind veer  
**23** away from the wind direction in geostrophic equilibrium is (i) due to direct fric-  
**24** tional effects in the very vicinity of the surface and (ii) due to turbulence which  
**25** exerts indirect frictional effects; these effects cause a slow-down of the mean wind  
**26** reducing the Coriolis force thus turning the wind in favor of the pressure gradient  
**27** force. Not only does the veering set the frame of reference for surface layer theory,  
**28** it also has effects at small and large scales from large-scale dispersion via plume  
**29** spreading to cyclone spin-down (Svensson and Holtlag 2009) and on the capa-  
**30** bilities of data assimilation and accuracy of surface flux estimates (Brown et al.

<sup>1</sup> FU Berlin, Institut für Meteorologie, Carl-Heinrich-Becker-Weg 6–10, 12165 Berlin, Germany  
cedrick@posteo.de

<sup>2</sup> Carl von Ossietzky Universität Oldenburg, School of Mathematics and Science, Institute of Physics

<sup>3</sup> ForWind - Center for Wind Energy Research, Küppersweg 70, 26129 Oldenburg, Germany

31 2005). From a large-scale perspective, the veering of wind across the planetary  
 32 boundary layer determines the amount of cross-isobaric mass-flux, commonly re-  
 33 ferred to as 'Ekman pumping' (Ekman 1905), and it is thus a key factor in the  
 34 life-cycle of large-scale synoptic systems. Within the atmospheric boundary layer  
 35 (ABL), directional shear of the wind in the upper part of the surface layer may  
 36 cause a systematic yaw for tall wind power generation devices where blades reach  
 37 into the Ekman layer, i.e. that part of the boundary layer where the wind starts to  
 38 turn; an exact estimate of such effects is critical in the site assessments for wind  
 39 farms (Calaf et al. 2010; Mirocha et al. 2018).

40 In the planetary boundary layer, wind veer is characterized by the surface  
 41 veering angle  $\alpha$  defined as the angle between the negative surface shear stress  $\tau_{\text{sfc}}$   
 42 and the geostrophic wind. Surface veering  $\alpha$  and geostrophic drag  $Z \equiv u_*/G$ , where  
 43 the friction velocity  $u_* \equiv \sqrt{|\tau_{\text{sfc}}|/\rho}$ , uniquely determine the surface drag  $\tau_{\text{sfc}}$  in a  
 44 turbulent Ekman flow. In any quantitative description of the surface layer, the  
 45 friction velocity  $u_*$  is the dynamic scale and  $\alpha$  defines the horizontal alignment  
 46 of the frame of reference, i.e. the rotation of the surface friction with respect  
 47 to the outer wind direction. Knowledge about  $u_*$  and  $\alpha$  is thus a prerequisite  
 48 for any quantitative theory of the surface layer, and Rossby and Montgomery  
 49 (1935) constrained the two parameters based on integral relations in the ABL.  
 50 Asymptotic similarity theory was later used by Tennekes (1973); Blackadar and  
 51 Tennekes (1968), and-based on his seminal direct numerical simulations (DNS)  
 52 of Ekman flow-, Spalart (1989) suggested a modification to take into account  
 53 effects of low to intermediate Reynolds numbers. Later on, constants were re-  
 54 evaluated with a focus on the ABL based on observations (Högström 1988, 1996)  
 55 and numerical modelling (Spalart et al. 2008, 2009; Ansorge and Mellado 2014;  
 56 Ansorge 2019).

57 Attempts were also undertaken to obtain profiles of the wind speed: One ap-  
 58 proach is to match the inner and outer layer at a reference height as usggested by  
 59 Etling (2002); Emeis (2018) (Sec. 21.10; Eq. 21.48); they choose the Prandtl-layer  
 60 height  $z_{\text{Prandtl}}$  to match the wind speed profiles, which, however, requires external  
 61 prescription of  $\alpha(z_{\text{prandtl}})$ , the veering at that height. A one-dimensional profile  
 62 with constant veering is given by Emeis et al. (2007, Sec. 3; Eq. 3.1-3.19).

63 Gryning et al. (2007) present an extension of the wind-speed profile beyond the  
 64 surface layer using a neutral reference profile and a stability correction; Kelly and  
 65 Gryning (2010), based on a probabilistic representation of stratification, develop  
 66 a model for the long-term mean wind speed in the ABL and compare this with  
 67 observation at different sites; Kelly and Troen (2016) demonstrate the effect of  
 68 such improved model for wind-energy applications. In consideration of the large  
 69 scale separation in geophysical flow, the rotation of the wind in the surface layer is  
 70 often assumed negligible, and above investigations merely focus on the wind speed;  
 71 that means, the veering of the wind with height is not described and there is little  
 72 knowledge on the profile of the span-wise velocity component and the precise  
 73 shape of the hodograph in the limit of a truly neutral Ekman boundary layer. A  
 74 climatology of wind turning in the ABL is given by Lindvall and Svensson (2019)  
 75 Klein et al. (2021) use a statistical turbulence modelling approach that yields a  
 76 two-component velocity profile, but they also find that the exact representation of  
 77 turning is challenging.

78 Ekman-layer models are roughly based on Ekman's seminal 1905 paper in  
 79 combinations with additional assumptions. One option is a prescribed profile shape

for eddy viscosity (Ellison (1955)), another are two-layer models of the ABL that take into account rotational effects at higher altitudes, for instance when the wind speed needs to be evaluated at heights on the order of 100 – 200 m, a particular concern when it comes to wind-power forecasting (Etling 2002; Emeis 2018; Optis et al. 2014). Despite rotational effects being considered, the formulation of these models for the outer layer and analysis of their performance primarily focuses on wind speed. Still, in 2018, Jiang et al. recognized that the outer part of the Ekman boundary layer receives less attention in comparison with the surface layer and study the neutral problem by Large-Eddy simulation (LES). They focus on the wind speed and find an extended logarithmic layer when considering the wind speed instead of the shear-aligned component, and they eventually demonstrate by means of an analytical model that this vertical extension of the logarithmic layer may be explained by a transfer of stress to the span-wise velocity component where it is assumed that the shear vector  $\tau(z)$  and stress vectors  $(\partial_z U, \partial_z V)$  are aligned.

More recently, Ghannam and Bou-Zeid (2021) treated the horizontally averaged momentum budget to show that departures from shear-alignment in the vicinity of the surface result in an integral of the wind veer ( $\alpha_M$  in their notation) over the height to very high accuracy ( $\int_{z_0}^H \sin \alpha_M$  in their notation; their Eq. (16)). Classic surface-layer similarity is recovered when the angle  $\alpha_M$  does not depend on height, i.e., the wind veer is constant across the surface layer. If, however, the wind veer depends on height, the profiles of stress and mean velocities depart from the scalings implied by classic surface-layer similarity.

Turbulent Ekman flow is considered here as a conceptual model of the homogeneous, stationary ABL over a flat surface under neutral stratification. Universal profiles of the wind vector for turbulent Ekman flow not only are a well-described limit for theoretical exploration or higher-order approaches taking into account possible effects of stratification, roughness or other physical complications encountered in the real geophysical system. While, on first sight, the study of such a strongly idealized case appears as an academic problem, it contains the essence of surface similarity as it is used in most atmospheric models, be it conceptual or numeric ones. More complex accounts generally refer to the homogeneous stationary problem as a base state: (i) Roughness is commonly incorporated by a linear transformation of vertical scale involving the roughness parameter  $z_0$  and for larger roughness also a displacement height (Monin and Yaglom 1975; Jacobs and Van Boxel 1988; Högström 1988); (ii) Stability can be accounted for by a linearization around the neutrally stratified profile (Monin 1970; Monin and Yaglom 1975; Högström 1988, 1996; Sakagami et al. 2020); (iii) Non-stationarity in the pressure-gradient forcing can be accounted for by a linear damped-oscillator approach around the base state (Momen and Bou-Zeid 2016); (iv) Barotropic and baroclinic effects on the velocity profile require to consider the height-dependence of the veer and stress misalignment (Momen et al. 2018; Ghannam and Bou-Zeid 2021). Furthermore, such a solution can serve as better initial condition for numerical simulation of the flow, to minimize the length of initial transient periods, or as benchmark for turbulence closures that can be tuned to reproduce the neutral limit case.

Despite the strong simplifications implied by our choice of set-up, there is no straightforward approach to solving this well-defined problem. Large-Eddy simula-

tion not only needs to be tuned for the surface shear stress and veering angle, but it also relies on sub-grid closures that commonly assume alignment of the turbulent stress with gradients. This pre-requisite is not fulfilled when the wind rotates with height. Esau (2004) investigated the representation of the Ekman boundary layer by dynamical subgrid closures and Zikanov et al. (2003) proposed a closure for the wind profile using a linearized representation of the eddy viscosity. Despite advances in analysis of this simplified set-up (Jiang et al. 2018), there is yet insufficient understanding for a quantitative generalization of the results to arbitrary external forcing (manifest in variation of the Reynolds number) – and indeed the fundamental questions pertaining to such relatively simple dynamics of turbulence are not reflected in the research on LES for the ABL over the past 50 years (Stoll et al. 2020).

At the same time, an increasing amount of high-quality and high-resolution data from turbulence-resolving approaches is emerging due to recent advances in high-performance computing and its application to geophysical problem sets; the geophysical range of scale separation, however, is—and it will remain so for the foreseeable future—out of reach for such simulation (Dimotakis 2005). Here, the routinely employed concept of Reynolds-number similarity can help. It postulates the existence of *fully developed turbulence* believed to occur for a sufficiently large but finite Reynolds number (Barenblatt and Goldenfeld 1995). (Already in 1998, this in fact lead Moin and Mahesh to the question *how high a Re is high enough?*) Certain statistics of fully developed turbulence, such as dissipation (Dimotakis 2005) or profiles of mean velocity (Barenblatt 1993), become independent of the Reynolds number when appropriately scaled; other statistics, such as the near-wall maximum in velocity fluctuation depend on Re (Baars and Marusic 2020) and externality of the flow may exert an impact on near-wall scaling (da Silva et al. 2014). It appears that for certain statistics in Ekman flow, fully-developed turbulence is reached with the Reynolds numbers that became possible due to an increase of computing capabilities over the past decades.

This paper exploits the robust features of mean velocity profiles from direct numerical simulation across a range of Reynolds numbers to formulate both the streamwise and span-wise components of the mean velocity vector as a function of the Reynolds number.

## 161 2 Problem formulation and numerical approach

162 We consider here incompressible, turbulent Ekman flow, that is, the turbulent flow  
 163 over a flat rotating plate, as a physical model for the truly neutral ABL. The f-  
 164 plane approximation is applied such that rotation only acts on horizontal velocity  
 165 components; we thus neglect rotational effects on the horizontal components of  
 166 velocity and dynamical effects due to latitudinal variation of the rate of rotation.

### 167 2.1 Notation and governing equations

168 The dimensional velocity vector of the numerical simulations is  $\underline{U} = (U_1, U_2, U_3) =$   
 169  $(U, V, W)$  over the coordinate system  $Oxyz$ , where an approximate alignment (plus/  
 170 minus few degrees) of the direction  $Ox$  with the surface shear stress is achieved. We

171 consider velocity profiles only, i.e. all velocities are averaged over horizontal planes  
 172 and in time, that is, they correspond to an Ensemble average. The coordinate  $Oz$   
 173 points away from the wall, and  $Oy$  points in the span-wise direction normal to  
 174  $Oxz$ . For analysis of the results, we use two coordinate systems that are (i) exactly  
 175 aligned with the surface shear stress

$$\underline{\tau}_{\text{sfc}} = \begin{pmatrix} \tau_x \\ \tau_y \\ \tau_z \end{pmatrix} = -\nu \left( \frac{\partial U}{\partial z} \hat{e}_x + \frac{\partial V}{\partial z} \hat{e}_y \right) \quad (1a)$$

176 and labelled by an upper index  $\alpha$  as in  $\underline{U}^\alpha$  for the velocity vector, and (ii) the  
 177 coordinate system aligned with the free-atmosphere geostrophic wind labelled by  
 178 an upper index  $G$  as in  $\underline{U}^G$ . We denote the square root of the modulus of surface  
 179 shear, the surface friction, by

$$u_* = \sqrt{\|\underline{\tau}_{\text{sfc}}\|} \quad (1b)$$

180 and let  $Z_* = G/u_*$ ; the surface veering angle  $\alpha_*$  is the angle between  $\underline{\tau}$  and the  
 181 geostrophic wind

$$\alpha_* = \sphericalangle(\underline{G}, \underline{\tau}_{\text{sfc}}). \quad (1c)$$

182 Analogously, we denote the height-local veering of the wind  $\alpha(z) = \sphericalangle(\underline{G}, \underline{U}(z))$ ,  
 183 where  $\underline{G} = (G_1, G_2, 0)$  is the geostrophic wind vector.

184 We consider the incompressible Navier–Stokes equations for the three velocity  
 185 components on the f-plane in a framework that is governed by (i) geostrophic wind  
 186 magnitude  $G = \sqrt{G_1^2 + G_2^2}$ , (ii) Coriolis parameter  $f$  (representing the angular  
 187 rotation), and (iii) kinematic viscosity  $\nu$ . In absence of external variability, this  
 188 system converges to a statistically steady state in the sense that flow statistics  
 189 do not depend on time; and this state is defined by a Reynolds number, the only  
 190 non-dimensional parameter that governs the system. We use the geostrophic wind  
 191 as velocity and the Coriolis parameter  $f$  as time scale for the non-dimensional  
 192 framework. This implies the Rossby radius  $A_{\text{Ro}} = G/f$  as length scale, such that  
 193 one Reynolds number governing the problem reads as

$$\text{Re}_A = \frac{GA_{\text{Ro}}}{\nu}. \quad (2)$$

194 The scales used in defining  $\text{Re}_A$  are of limited relevance for description of the  
 195 turbulent flow state. The turbulence scale separation in a wall-bounded flow is  
 196 commonly characterized by the friction Reynolds number (Jiménez 2012):

$$\text{Re}_\tau = \frac{u_* \delta}{\nu} = \delta^+ = \frac{\text{Re}_A}{Z_*^2}, \quad (3)$$

197 where  $\delta = u_*/f$  and we use a superscript '+' to denote normalization by inner tur-  
 198 bulence scales  $(u_*, \nu)$ . Another common measure of scale separation is the Reynolds  
 199 number  $\text{Re}_D = GD/\nu$  defined by the laminar Ekman layer thickness  $D = \sqrt{2\nu/f}$ .

200 The governing equations non-dimensionalized by  $G$ ,  $f$ , and  $A_{\text{Ro}}$  read as

$$\frac{\partial u_i}{\partial t} = \frac{\partial \pi}{\partial x_i} - u_j \frac{\partial u_i}{\partial x_j} + \epsilon_{i2j}(u_j - g_j) + \frac{1}{\text{Re}_A} \frac{\partial^2 u_i}{\partial x_j^2} \quad (4a)$$

$$\frac{\partial u_j}{\partial x_j} = 0, \quad (4b)$$

**Table 1** Direct numerical simulation data sets used in this work.  $Re_A$  and  $Re_D$  refer to the Reynolds number defined in terms of the Rossby radius  $\Lambda$  and Ekman-layer thickness  $D$  respectively.  $L_{xy}$  is the domain size in the stream- and span-wise direction. The grid is given by the number of grid points in the stream-wise ( $N_x$ ), span-wise ( $N_y$ ) and vertical ( $N_z$ ) directions respectively. The resolution in the span-wise and stream-wise directions are given as  $\Delta x^+$  and  $\Delta y^+$ . The grid in the vertical is stretched, and resolution at the wall is given by  $\Delta z^+$ .

$Re_A$	$Re_D$	$L_{xy}/\Lambda$	$N_x \times N_y \times N_z$	$\Delta x^+$	$\Delta y^+$	$\Delta z^+ _{z=0}$
125 000	500	1.08	$2048 \times 2048 \times 192$	4.1	4.1	1.05
281 250	750	1.08	$3072 \times 3072 \times 384$	5.6	5.6	1.60
500 000	1 000	1.08	$3072 \times 6144 \times 512$	9.3	4.7	1.14
845 000	1 300	0.54	$2560 \times 5120 \times 640$	8.9	4.5	0.99
1 280 000	1 600	0.54	$3860 \times 7680 \times 960$	8.6	4.3	1.00

**Table 2** DOIs and reference to the openly accessible data set at refubium repository

$Re_D$	DOI	Reference
500	<a href="https://doi.org/10.17169/refubium-42505">10.17169/refubium-42505</a>	Ansorge (2024a)
1000	<a href="https://doi.org/10.17169/refubium-42507">10.17169/refubium-42507</a>	Ansorge (2024b)
1300	<a href="https://doi.org/10.17169/refubium-42508">10.17169/refubium-42508</a>	Ansorge (2024c)
1600	<a href="https://doi.org/10.17169/refubium-42509">10.17169/refubium-42509</a>	Ansorge (2024d)

201 where  $u_i = U_i/G$  are the non-dimensional components velocity,  $\pi$  is non-dimen-  
 202 sional pressure,  $g_j = G_j/G$  are non-dimensionalized components geostrophic wind  
 203 (with  $g_1^2 + g_2^2 = 1$  by construction), and  $\epsilon$  is the Levi–Civita tensor. These equations  
 204 are solved inside a bounded cube of size  $L_x \times L_y \times L_z$  with periodic boundary condi-  
 205 tions in the lateral (streamwise and spanwise) directions, a no-slip–no-penetration  
 206 boundary at  $z = 0$ , and a no-penetration, free-slip boundary at  $z = L_z$ .

## 207 2.2 Numerical simulations

208 The problem is solved numerically by tLab<sup>1</sup>, an open-source tool-suite to simulate  
 209 and analyze turbulent flows. We use here a fourth-order–five-step Runge–Kutta  
 210 integration and sixth-order compact schemes for spatial derivatives in all direc-  
 211 tions. The incompressibility constraint is enforced by a fractional step approach  
 212 where the Poisson equation for the pressure field is solved to machine accuracy  
 213 using a combined spectral/compact approach as described in Mellado and Ansorge  
 214 (2012).

215 Simulations used here are shown in Tab. 1. We extend an existing set of simula-  
 216 tions for  $Re_A \in \{125\,000; 281\,250; 500\,000\}$  (gray shading; cf. Ansorge and Mellado  
 217 2014, 2016) by new simulations at higher Reynolds numbers up to  $Re_A = 1.28 \times 10^6$   
 218 with a horizontal domain extent up to  $3.3 \times 10^4$  viscous units. In total, this yields  
 219 one order of magnitude variation in terms of the scale separation in the boundary  
 220 layer.

<sup>1</sup> <https://github.com/turbulencia/tlab>

---

**221 3 Scaling behavior of the flow for  $\text{Re}_\tau$  up to 3000**

222 The generalization of profiles to arbitrary Reynolds numbers requires sufficient  
 223 scale separation in the simulations, not only to quantify the effect of the Reynolds  
 224 number on low-order flow statistics, but also to assess the corresponding rate-of-  
 225 change to eventually allow for an extrapolation of the findings. While the simula-  
 226 tions previously available (gray shading in Tab. 1) give confidence in a first-order  
 227 representation of the turbulent problem, the estimation of higher-order effects such  
 228 as the dependency of the Reynolds number requires a broader scale separation that  
 229 is made available by the two new simulations at increased Reynolds number (cf.  
 230 Tab. 1). Data at such scale separation has been obtained previously (cf. Spalart  
 231 et al. 2008, 2009), but we also need high confidence with respect to the convergence  
 232 of simulation data for slow oscillations and with respect to sampling convergence,  
 233 which translates to two further requirements on the data: First, data should be free  
 234 of artifacts from long-term oscillations across the vertical extent of the domain—  
 235 primarily, simulations should be free of effects originating from the inertial oscil-  
 236 lation; this is achieved here by replacing the mean value of the three-dimensional  
 237 velocity fields by the time mean over a whole inertial oscillation. Second, high  
 238 accuracy is also needed in terms of the statistical convergence of averages, bulk  
 239 measures and large-scale structures; this requires a domain size  $L_x > \mathcal{O}(\delta_{95})$ . We  
 240 use here  $L_x = L_y = 1.08\Lambda$  for cases with  $\text{Re} \leq 1000$  and  $L_x = L_y = 0.54\Lambda$  for  
 241  $\text{Re} \geq 1300$  which corresponds to  $L_x/\delta_{95} \approx 25$  for  $\text{Re}_D = 500$  and  $L_x/\delta_{95} \approx 18$  for  
 242  $\text{Re}_D = 1300$ .

243 Bulk parameters of the simulations are given in Tab. 3. The surface stress is  
 244 characterized by  $u_*$  and  $\alpha_*$  in relation to the geostrophic wind vector and dis-  
 245 cussed in more detail as the drag law below in Sec. 4.1 (we find the expected slight  
 246 decrease of  $u_*/G$  and  $\alpha_*$  with increasing  $\text{Re}$ ). The boundary-layer height estimated  
 247 from the 95% stress reduction,  $\delta_{95}$ , is around  $0.6\delta$  to  $0.66\delta$ . Interestingly, the in-  
 248 tegrated TKE  $\int_0^\delta edz$  stays constant when normalized by the friction velocity  $u_*$   
 249 while the integrated dissipation  $\int_0^\delta edz$  exhibits inviscid scaling when normalized  
 250 by the magnitude  $G$  of the geostrophic wind. (TKE and dissipation normalized  
 251 as  $fG^{-3} \int edz$  and  $u_*^{-3} \int edz$ , exhibit substantial dependence on  $\text{Re}$  for the vari-  
 252 ation of  $u_*$ .) This indicates that the bulk dissipation is governed by the forcing  
 253  $G$ -irrespective of  $\text{Re}$ . Changes in  $\text{Re}$ , however, affect the level and organization of  
 254 turbulence, and the parameter representing this dependency is the friction veloc-  
 255 ity  $u_*$  which describes the turbulence production processes in the surface layer, in  
 256 particular in the buffer layer.

257 Velocity profiles in inner units ( $U^{\alpha+}(z^+)$ , Fig. 1a) and outer units ( $U^{\alpha-}(z^-)$ ,  
 258 Fig. 1b) are in accordance with previous work (Coleman et al. 1992; Spalart et al.  
 259 2008, 2009; Ansorge and Mellado 2014; Ansorge 2019): The profiles of the shear-  
 260 aligned streamwise velocity component are well-collapsed for  $\text{Re}_D > 500$  below  
 261  $z^- \approx 0.15$  (circles in Fig. 1a); the case with  $\text{Re}_D = 500$  is only transitionally  
 262 turbulent and there is no distinct inner-outer scale separation. The logarithmic  
 263 law is appropriate for  $50 < z^+ < 0.15\text{Re}_\tau$ , where  $z^+ = \text{Re}_\tau z^-$ . While the pro-  
 264 files  $U^{\alpha+}(z^+)$  diverge between different  $\text{Re}$  beyond  $z^- = 0.15$ , the corresponding  
 265 profiles of the velocity deficit ( $U^{\alpha+}(z^-) - G_1^\alpha$ ) agree closely, irrespective of  $\text{Re}$ .  
 266 This illustrates the inner–outer scale-duality in this external flow with inner scal-  
 267 ing being appropriate in the inner layer and outer scaling in the outer layer. Also

**Table 3** Bulk characterization of the simulations for different Reynolds numbers Viscous Reynolds number  $\text{Re}$ , friction Reynolds number  $\text{Re}_\tau$ , friction velocity  $u_*$ , surface veering angle  $\alpha_*$ , normalized boundary layer depth  $\delta_{95}/\delta$ , inner normalization of vertically integrated TKE, outer normalization of vertically integrated dissipation.

$\text{Re}$	$\delta^+ = \text{Re}_\tau$	$u_*/G$	$\alpha_*$	$\delta_{95}/\delta$	$f u_*^{-3} \int_0^\delta \epsilon dz$	$G^{-3} \int_0^\delta \epsilon dz$
500	479	0.0619	25.5	0.66	0.88	1.31
750	886	0.0561	21.0	0.65	0.90	1.34
1000	1403	0.0530	18.8	0.62	0.92	1.30
1300	2122	0.0501	17.9	0.59	0.85	1.24
1600	2978	0.0482	17.2	0.61	0.91	1.21

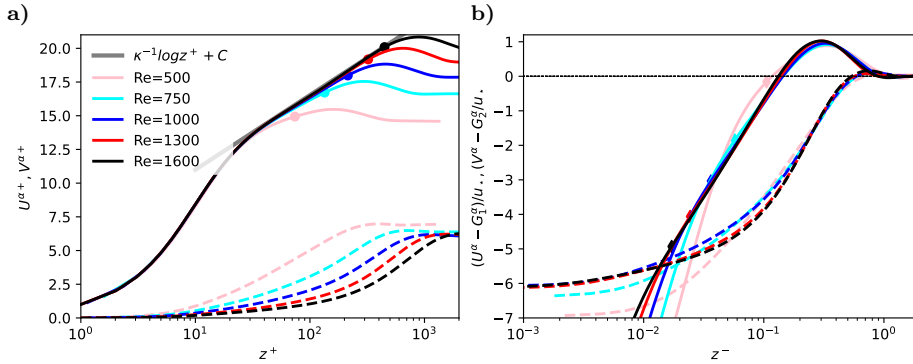


**Fig. 1** a) Shear-aligned velocity profiles in inner units; circles mark the height  $z^- = 0.15$ ; b) Shear-aligned velocity deficit in outer units; diamonds mark the grid point closest to the height  $z^+ = 50$

in the outer layer of the flow,  $u_*$  (and not the magnitude of the geostrophic wind  $G$ ) governs the inviscid normalization, i.e. a scaling independent of the Reynolds-number.

No collapse is found for the profiles of spanwise velocity when considered in inner units,  $V^{\alpha*+}(z^+)$ . When normalized in outer units, the deficit profiles of spanwise velocity  $(V^{\alpha*}(z^-) - G_2^\alpha)/u_*$  agree well beyond  $z^- \approx 0.3$ . This is a much higher level in comparison with the streamwise component that collapses also within the overlap layer, i.e. much closer to the surface (circles in Fig. 1b). The value of  $V^{\alpha*+}(z^-) - G_2^\alpha$  is sensitive to the wind veering for  $z \rightarrow 0$  as—for use of the shear-aligned component—it has to approach the value  $-G_2^\alpha = |G| \sin \alpha \neq 0$  in view of the no-slip boundary condition. While low-Re effects appear to be present for  $\mathcal{O}(\text{Re}) < 10^3$ , the spanwise component converges to an Re-independent limit within the range of scale separation considered here, i.e.

$$G_2^\alpha/u_* = Z_* \sin \alpha \rightarrow \text{const. for } \text{Re} \rightarrow \infty, \quad (5)$$

which has indeed already been found by Spalart (1989), who estimates the constant from an integral relation.

The viscous stress

$$S_{\text{visc}} = \nu \sqrt{\left( \frac{\partial U}{\partial z} \right)^2 + \left( \frac{\partial V}{\partial z} \right)^2} \quad (6a)$$

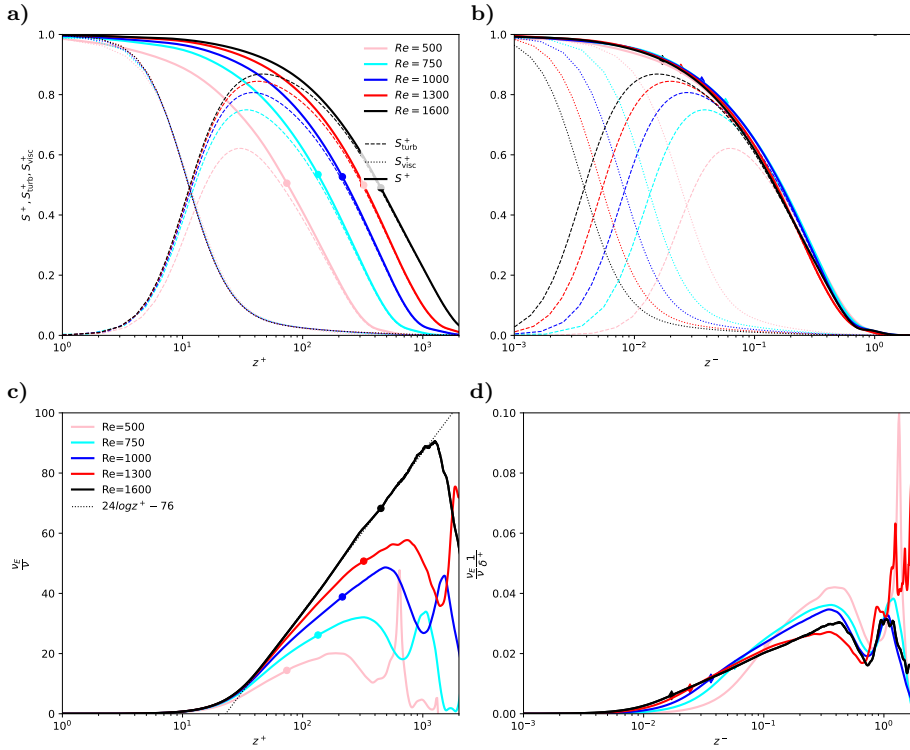


**Fig. 2** **a-b)** Profiles of the turbulent stress  $S_{\text{turb}}^+$  (dashed), the viscous stress  $S_{\text{visc}}^+$  (dotted), and the total stress,  $S^+ = S_{\text{visc}}^+ + S_{\text{turb}}^+$  (solid) as a function of inner height **(a)** and outer height **(b)**. **c-d)** Normalized eddy viscosity  $\nu_E$  (solid) plotted versus inner height **(c)** and outer height **(d)**. **(c)** uses inner normalization; **(d)** uses normalization by  $\delta^+$  which approximately collapses data in the outer layer. Different colors are for different Reynolds numbers (cf. Tab. 1). Circles in **(a)** and **(c)** denote the height  $z^- = 0.15$ , diamonds in **(b)** and **(d)** are for  $z^+ = 50$  as in Fig. 1

exhibits universal scaling when considered as  $S_{\text{visc}}^+(z^+)$  (Fig. 2a); this normalization is also appropriate in the outer layer where the viscous stress is, however, small. Small deviations from the universal profile are observed for the smallest Reynolds number  $Re = 500$ ; we attribute these to low-Re effects in the only transitionally turbulent flow ( $Re_\tau = 479$ ). In contrast to the viscous stress, the total stress follows outer normalization, i.e.  $S^+(z^-)$  is universal; a discrepancy in the inner layer does not occur as the total stress is approximately constant in the viscous and buffer layer, and a rescaling of the height would have no effect there; above, outer scaling is appropriate for the well-established dynamics in the overlap region of inner and outer layer. This, however, implies a mixed scaling for the turbulent stress,

$$S_{\text{turb}} = \sqrt{\overline{u'w'}^2 + \overline{v'w'}^2}, \quad (6b)$$

where dashed quantities  $u'$ ,  $v'$ ,  $w'$  indicate deviations from the mean and the overbar denotes horizontal and time averaging. Indeed,  $S_{\text{turb}}$  only follows inner normalization below  $z^+ \lesssim 20$  (where the turbulent contribution is negligible). In

298 the outer layer, where  $S_{\text{visc}} \rightarrow 0$ ,  $S_{\text{turb}}^+$  follows outer normalization for  $z^- \gtrsim 0.15$ —  
 299 with increasing accuracy for larger  $\text{Re}$  and larger distance from the surface. In the  
 300 overlap region, i.e. for  $z^+ > 20$  and  $z^- < 0.15$ , the mixed scaling for the turbulent  
 301 stress can be expressed as

$$S_{\text{turb}}^+(z^+, \text{Re}_\tau) = S^+(z^-) - S_{\text{visc}}^+(z^+), \quad (6c)$$

302 where  $z^- = z^+/\text{Re}_\tau$ .

303 The Eddy viscosity plays a crucial part when modelling profiles and the vertical  
 304 transport in turbulent flow. In analogy to the Fick-law for molecular diffusion, the  
 305 eddy diffusivity is the effective diffusivity that yields the turbulent transport  $S_{\text{turb}}$   
 306 based on the strain rate. For the symmetries in the flow (horizontal homogeneity,  
 307 and  $W = 0$ ), it is

$$\nu_E = \frac{S_{\text{turb}}}{\sqrt{\left(\frac{\partial U}{\partial z}\right)^2 + \left(\frac{\partial V}{\partial z}\right)^2}} = \nu \frac{S_{\text{turb}}}{S_{\text{visc}}}. \quad (7a)$$

308 The inner normalization of  $\nu_E$  is obtained when dividing by the molecular viscosity:

$$\nu_E^+ = \nu_E/\nu = S_{\text{turb}}/S_{\text{visc}}. \quad (7b)$$

309 Under this normalization, the profiles of eddy viscosity collapse below  $z^+ \approx 20$   
 310 with a tendency towards better collapse at higher  $z^+$  for higher Reynolds number  
 311 (up to  $z^+ \approx 50$  for  $\text{Re} = 1600$ ; Fig. 2c). In the outer layer, the eddy viscosity  
 312 is characterized by a distinct minimum at  $z^- \approx 0.6 - 0.8$ , and we find that the  
 313 following mixed normalization of  $\nu_E$  by the geostrophic wind and friction velocity  
 314 collapses the value of  $\nu_E$  at this minimum (cf. Fig. 2d):

$$\nu_E^- = \nu_E^+ \frac{1}{\delta^+} = \nu_E \frac{1}{\nu} \frac{\nu}{u_* \delta} = \nu_E \frac{f}{u_*^2}. \quad (7c)$$

315 Substantial variation of the profiles is, however observed below and above this  
 316 minimum for different  $\text{Re}$  which illustrates that this normalization is probably not  
 317 generally appropriate across the outer layer.

318 The organization of the flow with  $\text{Re}_\tau = 2978$  is depicted in terms of the  
 319 turbulence kinetic energy in Fig. 3. In vicinity of the wall, at  $y^+ \approx 10$ , (Fig. 3a),  
 320 elongated streaks aligned with the surface shear stress dominate. Moving away  
 321 from the wall, to  $y^+ \approx 150$  (well within the logarithmic region), the structures are  
 322 larger and more isotropic, but they are still largely aligned with the surface shear  
 323 stress. In the upper part of the outer layer, around  $y^+ \approx 1000$ , no clear signature of  
 324 the surface veering direction is found, and intense TKE structures (bright yellow)  
 325 are organized on a large spatial scale with weaker eddies (greenish structures) and  
 326 quiescent regions in between.

#### 327 4 A universal velocity profile for the turbulent Ekman layer

328 We now turn to the formulation of a general velocity profile that is fully determined  
 329 by the only parameter of the idealized problem, namely a Reynolds number repre-  
 330 senting the scale separation or geometric size of the problem. This precludes, first,  
 331 a drag law wherewith we begin this section (4.1). Based on the scaling arguments  
 332 put forward in Sec. 3, we then develop, second, a formulation of the wind vector

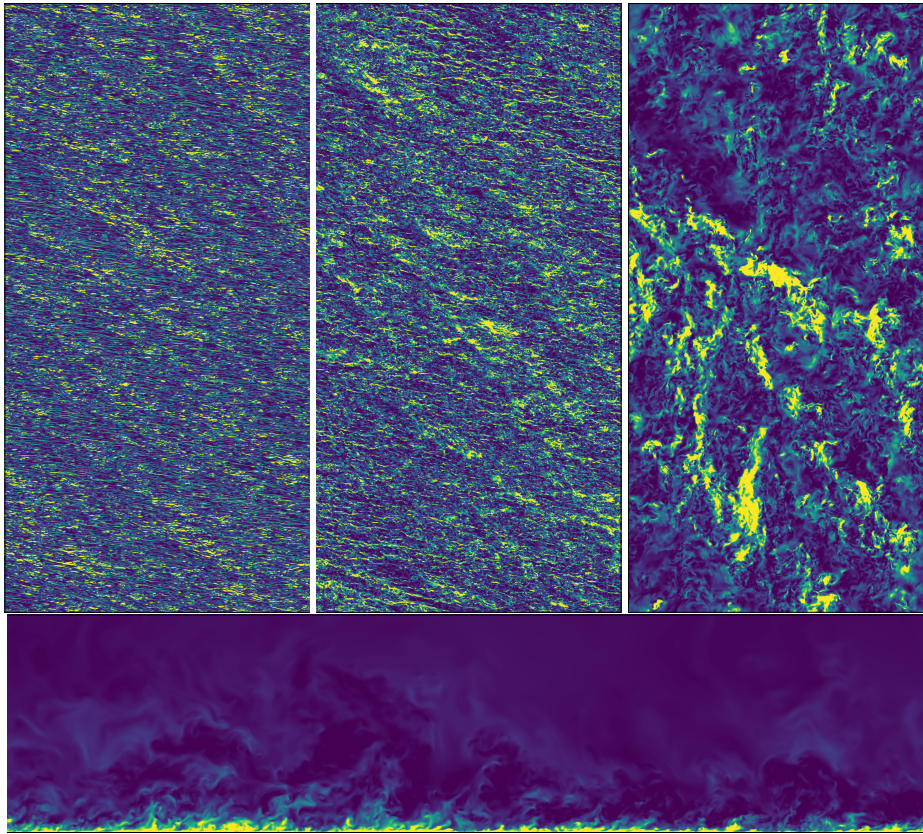


**Fig. 3** Horizontal slices of turbulence kinetic energy in the Buffer layer ( $i=10$ ), logarithmic Layer ( $i=100$ ), and outer layer ( $i=400$ ) of the case with  $Re_\tau = 2978$ ; coloring between percentiles 4 and 96 of the respective image. Lower panel: streamwise–vertical intersect through the domain

333 in the Ekman layer (Sec 4.2). Finally, we come up with a separate formulation of  
 334 the, third, stream-wise and, fourth, span-wise velocity components in the overlap  
 335 and inner regions of the flow.

336 4.1 Drag-law

337 A drag-law for Ekman flow determines—as a function of Reynolds number alone—  
 338 the surface drag. This can be formulated by the normalized surface friction,  $u_*$   
 339 (Eq. (1b), also termed geostrophic drag), and the direction of surface shear stress,  
 340  $\alpha_*$  (Eq. (1c), also termed wind veer). A non-zero veering of the wind is a rather  
 341 special case in comparison with most turbulent flows considered in an engineering  
 342 context, and it confronts us with a situation where the most appropriate coordinate  
 343 system for analysis (namely that aligned with the surface shear stress) is a priori  
 344 unknown. We compare our DNS data against a semi-empirical drag-law based on  
 345 integral consideration (Spalart 1989) and find, as demonstrated in previous work

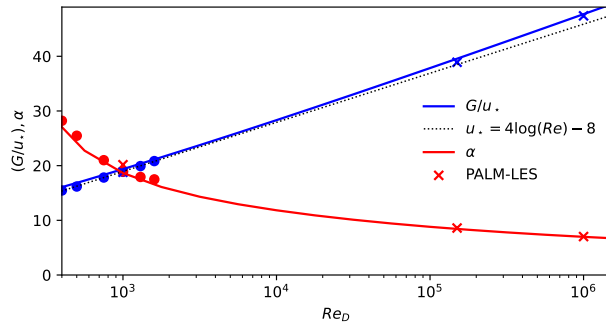


**Fig. 4** Variation of geostrophic drag,  $Z_*$ , and surface veering,  $\alpha_*$ , with Reynolds number according to the theory by Spalart et al. (1989) and as estimated from DNS data

(Ansorge and Mellado 2014), excellent agreement in the range  $400 < Re < 1600$ , representing a factor of 16 in variation of viscosity.

We also find that the solution of the transient equation involved in estimation of  $u_*$  for a given Reynolds number  $Re_D$  is approximated reasonably by the formulation

$$Z_* = 4 \log(Re_D) - 8 \quad (8)$$

which quantifies the ‘weak’ dependence of  $u_*$  on the Reynolds number as an approximately logarithmic one, at least for problems with a scale separation on the order that is relevant to geophysical problems ( $Re_D < 10^8$ ).

#### 4.2 Profile in the Ekman layer

Formulations for the outer layer that take into account the rotation (and thus deviation from the channel-flow analogy) need to be matched to the framework of surface similarity. A smooth transition from the inner layer to the Ekman layer, where the wind is characterized by a turning of its mean direction, is not easily achieved. Optis et al. (2014), for instance, define an “effective geostrophic wind vector that has the same magnitude of the observed surface geostrophic wind and is rotated by the angle  $\alpha$  [their nomenclature]” to overcome the unsteady transition when approaching the Ekman layer from below. Such rotation of the wind vector is *a posteriori* justified by the observational data that the model outcomes are compared to. This need for a connection of the two reference frames is a manifestation of a mismatch in the theoretical treatment of the inner and outer layer in this rotating flow configuration.

The text-book solution for Ekman flow makes use of the physical boundary conditions (BCs) for the ABL (no-slip at the bottom and geostrophic wind in the free atmosphere) and a constant eddy viscosity. Specifying the boundary conditions at top and bottom eliminates one mode of the analytical solution, and it determines the magnitude of the spiral. In doing so, one has to assume that the solution is appropriate across the entire ABL, which is not the case: The dynamics put forth by Ekman in 1905 are not appropriate in the surface layer of the ABL; better approximations exist for the logarithmic, buffer, and viscous sublayers. In view of this situation, we use an adapted Ekman spiral that does not enforce the

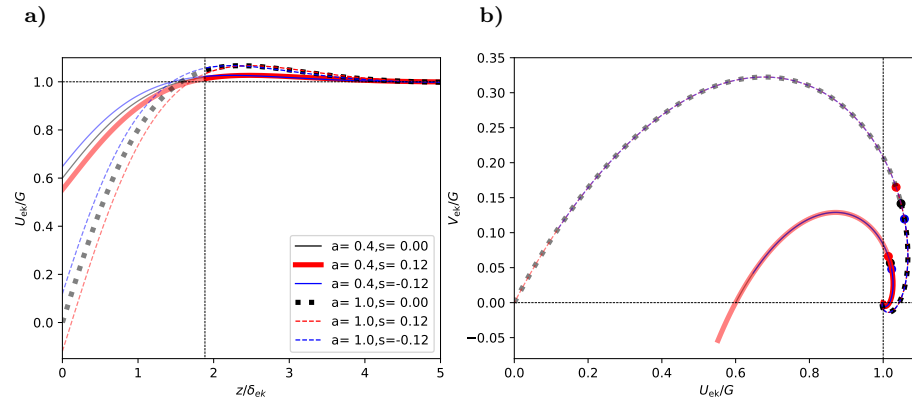


**Fig. 5** a) Generalized Ekman-profile of the geostrophic-aligned component  $U_{\text{ek}}$ . b) Hodograph for the geostrophic-aligned and pressure-gradient aligned components  $U_{\text{ek}}$  and  $V_{\text{ek}}$ . Thick, black dashed line shows the classic solution. The height corresponding to  $z^- = 0.30$  is marked by the dashed line in panel (a) and by filled circles in panel (b). The hodograph and profiles above this reference height are shown as solid lines, below as opaque line.

boundary conditions at the surface but at a different height. This is achieved by considering the Ekman spiral only in the Ekman layer, thus giving way for the well-established logarithmic and viscous-layer profiles in the lower surface layer. Based on the derivation in App. A, this profile is given by

$$\frac{1}{G} \begin{pmatrix} U_{\text{ek}} \\ V_{\text{ek}} \end{pmatrix} = \begin{pmatrix} 1 \\ 0 \end{pmatrix} + e^{-z_{\text{ek}}} \left[ a_{\text{ek}} \begin{pmatrix} -\cos z_{\text{ek}} \\ \sin z_{\text{ek}} \end{pmatrix} + b_{\text{ek}} \begin{pmatrix} \sin z_{\text{ek}} \\ \cos z_{\text{ek}} \end{pmatrix} \right]. \quad (9a)$$

with  $z_{\text{ek}} = \delta_{\text{ek}}(z^- - s_{\text{ek}})$ . The right-hand-side consists of two modes with magnitude  $a_{\text{ek}}$  and  $b_{\text{ek}}$  shifted by  $\pi/2$  with respect to each other. In the classic case, the second mode governed by  $b_{\text{ek}}$  is incompatible with the surface boundary condition. While this is not the case here for the general form of the profile, the phase shifts can also be captured by the parameter  $s_{\text{ek}}$ , and we stick with to a single-modal approach, i.e., we let  $b_{\text{ek}} = 0$ .

This single-modal solution is characterized by three parameters, (i) an Ekman-layer depth scale  $\delta_{\text{ek}}$ , (ii) the magnitude parameter of the spiral  $a_{\text{ek}}$ , and (iii) a zero-crossing point for the velocity  $s_{\text{ek}}$ . The effects of varying these parameters are illustrated in Fig. 5 where the classic Ekman solution is recovered by setting  $a_{\text{ek}} = 1$ ,  $s_{\text{ek}} = 0$  and  $\delta_{\text{ek}} = \sqrt{2\nu/f}$ . These parameters are *a priori* unknown as they need to conform to the turbulent state of the boundary layer; we use our DNS data to arrive at best estimates for them.

The **Ekman-layer depth scale**  $\delta_{\text{ek}}$  is fundamentally defined by the eddy viscosity. However, we have seen in Section 3 that a characteristic value for the eddy diffusivity is not easily obtained for its strong dependence on the Reynolds number and distance from the surface. We therefore resort to the physical manifestation of the eddy diffusivity in an Ekman layer, and use the boundary layer depth  $\delta_{\text{ek}} = 0.66\delta \times 2\pi$ . For the relation  $\delta_{\text{ek}} = \sqrt{2\nu_{\text{ek}}/f}$ , this yields  $\nu_{\text{ek}} \propto u_*^2/f$  in accordance with the observations in Sec. 3 (Eq. 7c).

The **magnitude parameter of the Ekman spiral**,  $a_{\text{ek}}$ , defines the super-geostrophic maximum of the wind profile aloft the logarithmic layer. Our simu-

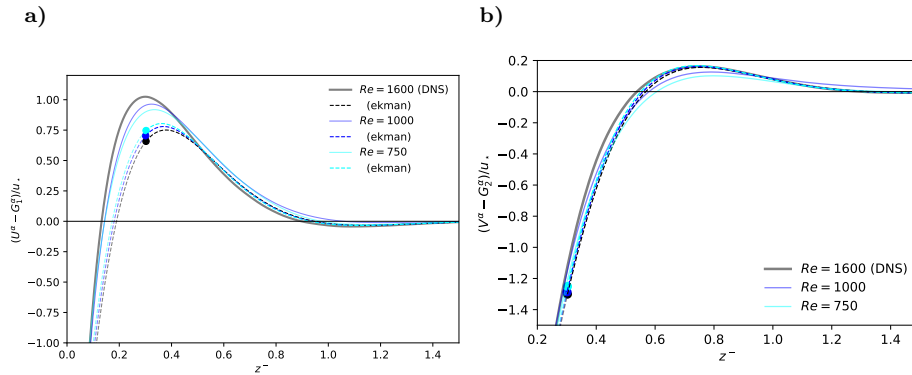


**Fig. 6** Shear-aligned velocity deficit for the streamwise (panel (a)) and spanwise (panel (b)) components of the mean velocity  $U^{\alpha}$  and  $V^{\alpha}$ . Solid lines show DNS data, dashed lines the Ekman profiles  $U_{\text{ek}}$  and  $V_{\text{ek}}$  as defined in Eq. 9. Variations in  $U_{\text{ek}}$  and  $V_{\text{ek}}$  are a consequence of the normalization and related to changes in  $u_{\star}$  and  $\alpha_{\star}$  among the different  $Re_D$ .

402 lations suggest this maximum of the velocity deficit remains constant when nor-  
 403 malized by  $u_{\star}$  as shown in Fig. 6. The numerical value of  $a_{\text{ek}}$  is estimated from  
 404 visual comparison, and we find  $a_{\text{ek}} = 8.4u_{\star}$ ; while this appears rather large, it is  
 405 pre-multiplied by  $e^{-z_{\text{ek}}}$  which has already decreased to  $\mathcal{O}(0.1)$  at the height of this  
 406 maximum. This choice ascertains that the velocity deficits  $U/u_{\star} - Z_{\star}$  and  $V/u_{\star} - Z_{\star}$   
 407 do not depend on the velocity scale  $u_{\star}$ , but only on  $G$  as

$$U_{\text{ek}}/u_{\star} - Z_{\star} \propto a_{\text{ek}}Z_{\star} = 8.4G. \quad (10)$$

408 **The offset parameter**  $s_{\text{ek}}$  defines the zero-crossing height of the profile (in  
 409 contrast to  $\delta_{\text{ek}}$ , which determines the thickness across which the wind veering  
 410 takes place). Physically, this offset can be understood as the height at which the  
 411 surface was located assuming a perfect Ekman flow down to the surface. As this  
 412 is not the case, and gradients are steeper in the highly turbulent boundary layer  
 413 flow encountered when approaching the surface, the offset is smaller than zero (the  
 414 fully turbulent boundary layer is actually thinner than an Ekman layer would be).  
 415 From our DNS data, we estimate  $s_{\text{ek}} = -0.12$ .

416 In summary, the outer layer of Ekman flow is characterized by a turning of  
 417 the wind velocity and the super-geostrophic maximum that is sustained by mo-  
 418 mentum convergence at the inflection point of the velocity profile. The super-  
 419 geostrophic maximum of streamwise velocity and a secondary minimum aloft the  
 420 bulk-turbulent part of the boundary layer are well-described by a classic Ekman  
 421 spiral with adapted boundary conditions and a shift in reference height. Corre-  
 422 sponding profiles are shown in comparison with data from three DNS runs in  
 423 Fig. 6. The idealized profiles capture the secondary minimum and convergence to  
 424 the geostrophic equilibrium in the non-turbulent flow very well.

#### 425 4.3 Streamwise velocity component

426 Well-established theories exist for the streamwise velocity profile, which in non-  
 427 rotating flows is aligned with the surface shear stress due to the geometry. These

428 theories cover various regimes based on their distance from the wall and the relative  
 429 influence of viscosity, turbulence, and interaction with the outer flow region, with  
 430 the logarithmic law for the mean velocity serving as a central reference point.

431 In immediate vicinity to the surface, local turbulent mixing cannot occur for  
 432 the no-slip/no-penetration boundary condition, and the mean velocity is described  
 433 by a viscous profile of the form

$$U^{\alpha_*+} = z^+ \quad (11a)$$

434 where the direction of the velocity points into the exact opposite direction of the  
 435 wall shear stress  $\tau$ . In absence of roughness elements and for small roughness  
 436 ( $z_0^+ < 5$ ), this linear regime is known as viscous sub-layer Foken (2002); Foken  
 437 et al. (1978). In fact, this law of the wall has no degree of freedom given the  
 438 drag, i.e. once  $u_*$  and  $\alpha_*$  are defined. However, theoretical foundation is lacking  
 439 for the exact shape of the velocity profile in the buffer layer; though crucial for  
 440 turbulence production, it is commonly understood as a transition region between  
 441 the linear profile at the surface and the logarithmic profile aloft. A pure blending  
 442 from the linear velocity profile into the logarithmic one is, however, not reasonable  
 443 as both the linear and logarithmic profile overestimate the velocity in the buffer  
 444 layer. We therefore introduce a two-step correction procedure, accounting for the  
 445 smaller-than linear growth beyond  $z^+ \approx 5$ , and assuring smooth matching with  
 446 the logarithmic law at  $z^+ = 40$ :

$$U_{\text{inner}}^{\alpha_*+} = \frac{z^+}{1 + c_1(y^+)^2} + (c_2 z^+ - a_{\text{match}}) \frac{1 + \tanh[0.2(z^+ - 22)]}{2} + c_3 e^{-c_4(z^+ - 22)^2}. \quad (11b)$$

447 We use here

$$c_1 = 0.00185; \quad c_2 = 0.195; \quad c_3 = 0.4; \quad c_4 = 0.35.$$

448 The second and third terms on the right hand side vanish for  $z^+ \ll 22$ , and  
 449  $c_1 = 0.00185$  implies an approximately 5% correction at  $z^+ = 5$  and an 18.5%  
 450 correction at  $z^+ = 10$ . The second and third term on the R.H.S. of eq. (11b) are  
 451 an empirical fit to the velocity profiles observed in the buffer layer and appear  
 452 independent of the Reynolds number for the range observed here. The coefficient  
 453  $a_{\text{match}}$ , which has no effect in the viscous sublayer, is then used to match this  
 454 formulation to the logarithmic law employed above.

455 In the logarithmic region, we use the profile

$$U_{\log}^{\alpha_*+} = \frac{1}{\kappa} \log z^+ + C \quad (11c)$$

456 with the von-Kármán constant  $\kappa = 0.416$  and the boundary condition  $C = 5.4605$ .  
 457 For this logarithmic law,  $a_{\text{match}} = 3.569861$  for a matching at  $z^+ = 40$ .

#### 458 4.4 Spanwise velocity component

459 The background rotation and associated veering of the surface wind implies a  
 460 non-zero profile for the span-wise velocity which challenges the conventional as-  
 461 sumptions related to the channel-flow analogy: While the analogy with channel

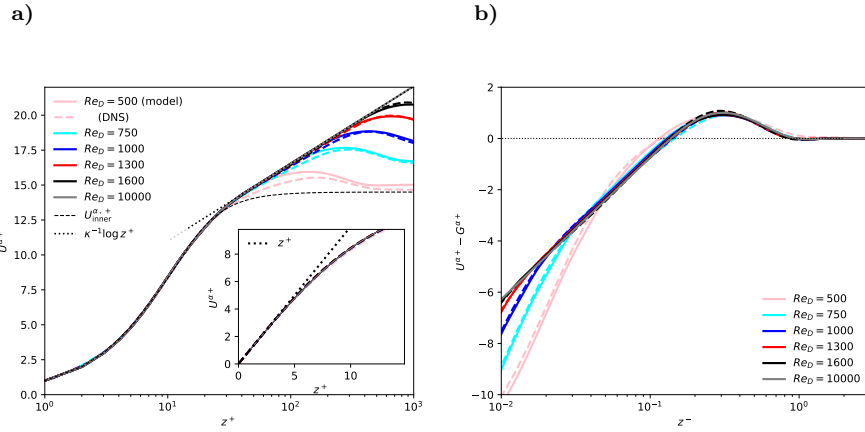


**Fig. 7** Shear-aligned profiles of velocity components  $U^{\alpha*+}$  in inner (left) and outer (right) units.

flow in vicinity of the wall implies that the streamwise component be zero or at least small, the veering requires a value of  $V_{top} = U_G \sin \alpha_*$  in the free stream (and thus also at the top of the boundary layer if we assume that any substantial velocity gradient is confined to the turbulent part of the flow). This continuous rotation of the wind vector is conveniently visualized by velocity hodographs aligned with the outer, geostrophic flow (cf. Fig. 5b) and normalized by the geostrophic wind. The geometry of the flow and its drag imply the following for any hodograph: (i) the boundary conditions at the surface, (ii) the boundary condition at the top, and (iii) the inclination of the hodograph at the origin by the surface veering:

$$V^{\alpha*}(z = 0) = 0, \quad (12a)$$

$$\lim_{z \rightarrow \infty} V^{\alpha*} = G \sin \alpha_* \quad (12b)$$

$$\partial_{z+} V^{\alpha*+} \Big|_{z=0} = 0. \quad (12c)$$

Outer scaling of the velocity profile further implies that the velocity deficit of  $(V^{\alpha*} - G^{\alpha*})/u_*$  be a universal function of the outer height  $z^-$ . In the outer region of the flow (for  $z^- \mapsto 1$ ),  $f_V(z^-)$ , should govern the spanwise velocity profile, as is supported by our DNS data (Fig. 1b); above  $z^- \approx 0.3$ , this profile is very well approximated by the Ekman-turning derived above (Eq. (9); Fig. 6b). While this deficit is a signature of outer rotation, it is inappropriate to extend this general relation to the surface where inner scales matter: On the one hand, the variation of the spanwise velocity deficit across the boundary layer (i.e. between  $0 < z^- < 1$ ) must match the difference implied by the drag law ( $u_*, \alpha_*$ ) and the constant value of  $V^{\alpha*}$  around  $z^- = 0.3$ . On the other hand, provided the outer velocity deficit is Re independent—the Re-dependence of  $\alpha_*$  and  $u_*$  implies that this difference cannot be constant as a function of Re. We hence ask, how does the span-wise component scale when the surface is approached? Clearly, the spanwise contribution is small in comparison with the streamwise component throughout much of the layer below  $z^- \approx 0.3$ . However, we cannot assume  $V = 0$  if a smooth matching between the inner and outer layers shall be achieved. In this context, we first realize that the velocity deficit  $(V^{\alpha*} - G^{\alpha*})/u_*$  approaches a Re-independent

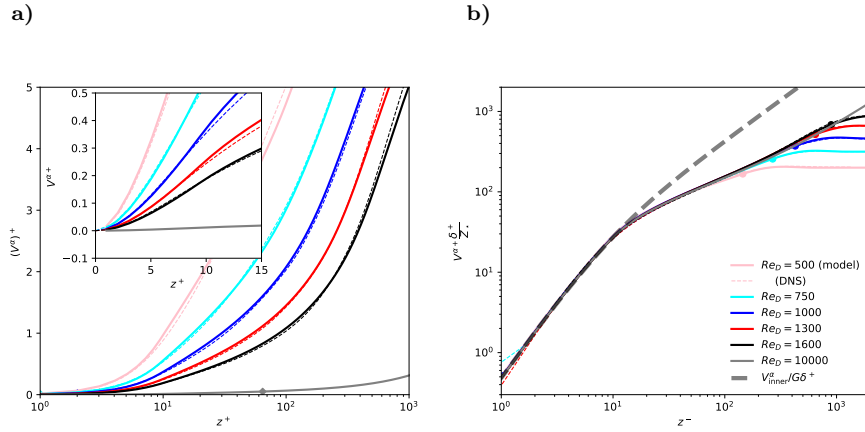


**Fig. 8** Profiles of shear-aligned span-wise velocity  $(V^\alpha)^+$  versus inner height. Dashed lines show DNS data, thick, opaque lines are from the semi-empirical theory developed above. Panel (a) shows standard inner normalization, panel (b) the inviscid normalization yielding a universal profile for the spanwise component of velocity in the inner layer.

constant around  $C_{V0} = Z_* \sin \alpha = 6.1$  at the surface; deviations from this constant are only found for the lowest Reynolds numbers which is in accordance with the low-Re correction suggested by Spalart (1989). This constrains the wind veer, and it quantitatively shows that the decreasing wall friction manifest in an increase of  $Z_*$  exactly compensates the decrease of wind turning measured by  $\sin \alpha_*$ .

If the difference across the boundary layer is constant ( $C_{V0}$ ) vs.  $Re$ , the averaged gradient  $\partial_{z^+} V^{\alpha*+}$  of the spanwise velocity component must decrease as  $1/\delta^+$  with increasing  $Re_\tau$ . Hence, it should—at a fixed height—be  $V^{\alpha*} \propto (\delta^+)^{-1}$ . A profile that agrees with the constraints of the profile at the surface and exploits the dependence of  $V^{\alpha*}$  on  $\delta^+$  is

$$V^{\alpha*} \frac{\delta^+}{G} = f_{V,visc}(z^+) = v_{ref} (\omega_v z^+ - 1 + \exp[-\omega_v z^+]), \quad (13)$$

where  $v_{ref}$  controls the magnitude of the profile and  $\omega_v$  sets the height at which the profile transitions into an approximately linear one. We find excellent agreement with the DNS data for  $500 \leq Re_D \leq 1600$  below  $z^+ \approx 15$  with

$$v_{ref} = 18.85; \quad \omega_v = 0.2353$$

(cf. Fig. 8b).

For the adjacent surface layer, we find a log-like transition from the quasi-linear profile inner profile around  $z^+ = 10$  to a linear profile with increasing  $Re$  (Fig. 8b). We model this transition by

$$f_{V,\log}(z^+) = \frac{V_{\log}(z^+)}{G} \delta^+ = a_{\log} + b_{\log} \log z^+ + c_{\log} z^+. \quad (14)$$

This surface-layer profile matches the inner (viscous) scaling in vicinity of the surface to the outer (Ekman) scaling above  $z^- = 0.3$  when constrained by the

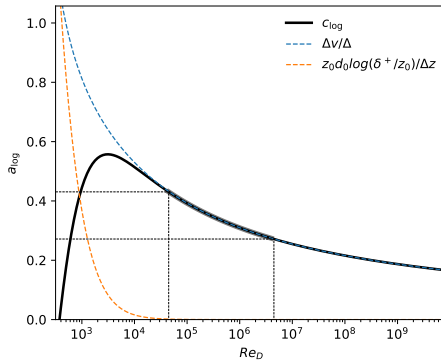


**Fig. 9** Coefficients  $a_{\log}$ ,  $b_{\log}$  and  $c_{\log}$  (cf. Eq. 14) as a function of the viscous Reynolds number  $Re_D$ . The approximate range of scale separation relevant for atmospheric application is found in between the dotted lines, where  $a_{\log} \simeq 0$  and  $c_{\log} \simeq 0.4$

507 viscous profile at the bottom and the Ekman profile at the top:

$$f_{V,\log}(z^+ = 10) = f_{V,\text{visc}}(z^+ = 10) =: v_{10} \simeq 27.3 \quad (15a)$$

$$\frac{\partial}{\partial z^+} [f_{V,\log}]_{z^+=10} = \frac{\partial}{\partial z^+} [f_{V,\text{visc}}]_{z^+=10} =: d_{10} \simeq 4.01 \quad (15b)$$

$$f_{V,\log}(z^+ = 0.3\delta^+) = V_{\text{ek}}^{\alpha*}(z^- = 0.3)\delta^+ =: v_{03} \quad (15c)$$

508 where  $v_{03}$  is determined by  $V_{\text{ek}}(0.3)$  and  $U_{\text{ek}}(0.3)$  and depends on  $Re$ . Given the  
 509 Ekman formulation of the velocity profile introduced in Sec. 4.2, one may express  
 510  $v_{03}$  using the Ekman profile introduced in Sec. 4.2 together with the approximation  
 511 for  $u_*(Re)$  found in Eq. (8). While the  $Re$ -dependency of  $a_{\log}$ ,  $b_{\log}$ ,  $c_{\log}$  is small,  
 512 it shows up in Fig. 1 where the normalized profiles of spanwise velocity become  
 513 more convex with increasing  $Re$ . We can now quantify this effect by means of the  
 514 change of  $c_{\log}$  versus  $Re$  which is shown in Fig. 9 (cf. Appendix B;  $a_{\log}$  and  $b_{\log}$   
 515 are then determined by the universal values of  $v_{10}$  and  $d_{10}$ ).

#### 516 4.5 Matching of the inner and outer layer profiles

517 The formulations introduced above are continuous across the transition from the  
 518 inner to the outer layer. However, the requirement of smooth derivatives would  
 519 over-constrain the velocity profiles and is hence not applied. This can, in particular  
 520 for low or extremely high  $Re$ , cause discontinuity in the derivatives of the velocity  
 521 profiles around the transition from the inner to the outer layer. To avoid such  
 522 artificial discontinuity, the profiles are blended by an error-function transition  
 523 using a blending height  $z_{\text{blend}}^- = 0.28 - 2.25\sqrt{1/Re_\tau}$  and a transition thickness  
 524  $z_{\text{trans}} = 2$ , such that the weighting function  $\omega(z^-)$  becomes

$$\omega(z^-) = \frac{1}{2} \left[ \text{erf} \left( z_{\text{trans}} \log \frac{z^-}{z_{\text{blend}}} \right) + 1 \right].$$

525 hence  $u_{\text{total}} = (1 - \omega) \times u_{\text{inner}} + \omega \times u_{\text{outer}}$  and similar for  $v$ .

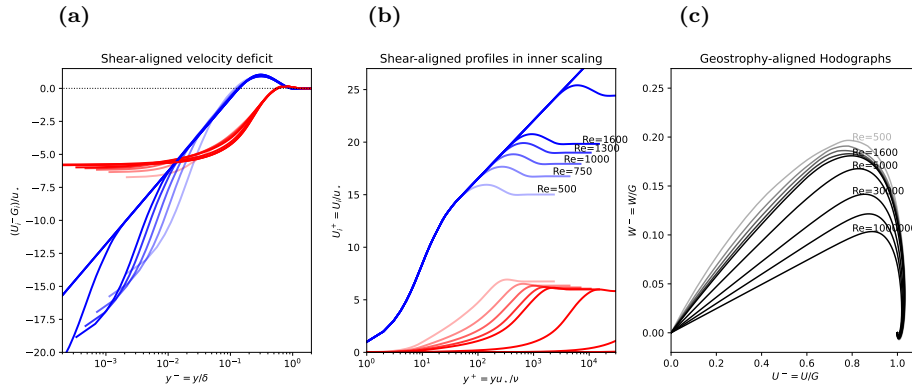


**Fig. 10** (a) Velocity deficit, (b) velocity profile in shear-aligned hodographs and (c) hodograph in geostrophy-aligned coordinates. In panels (a) and (b), blue lines correspond to the streamwise component and red to the spanwise.

526 The resulting velocity profiles across the entire boundary layer are shown in  
 527 inner and outer scaling as well as in hodograph-view in Fig. 10. The shear-aligned  
 528 velocity deficit is shown in outer scaling highlighting the universality in the outer  
 529 layer. The logarithmic scaling of the streamwise component is encountered as  
 530 straight blue lines in panels (a) and (b) where the extent of the logarithmic range  
 531 increases with  $Re$  towards lower values of  $z^-$  and higher values of  $z^+$  depending  
 532 on the scaling. Importantly, the logarithmic region is widening for increasing  
 533 Reynolds number – irrespective of the scaling. In this simple inner scaling, the  
 534 spanwise velocity (which follows a mixed scaling) does not collapse but seems to  
 535 depend on  $Re$  (the collapse is seen in Fig. 8). However, the velocity deficit in outer  
 536 units becomes approximately universal, also across the inner layer; this reflects  
 537 the compensation of reduced turning ( $\alpha$ ) by increased drag ( $u_*$ ), and is consistent  
 538 with the theoretical considerations discussed in 4.1.

539 The spanwise velocity at a fixed height scales approximately as  $Re_\tau^{-1}$  (Sec. 4.4).  
 540 However, the fraction of turning that is encountered within the inner layer of the  
 541 flow amounts to about 1/3 of the total wind veer (Fig. 12a). This is because, in  
 542 inner units, the inner layer grows as  $Re_\tau$  which exactly compensates the reduced  
 543 gradient of spanwise velocity. The hodographs show the well-known Ekman shape  
 544 with the laminar profile as an outer limit and 'flatter' hodographs, corresponding  
 545 to less turning, for increasing Reynolds number.

## 546 5 Discussion

### 547 5.1 Implications for surface-layer scaling

548 Eq. (13) establishes a universal mixed scaling for the spanwise velocity in the vis-  
 549 cous layer: While it requires the vertical coordinate to be expressed in inner units,  
 550 the velocity itself is normalized by the geostrophic wind, and becomes inversely  
 551 proportional to the friction Reynolds number  $Re_\tau = \delta^+$  when considered at a fixed  
 552 height. In vicinity of the surface, such mixed scaling has already been identified  
 553 for higher-order statistics in convective flows (Mellado et al. 2016; Li et al. 2018),

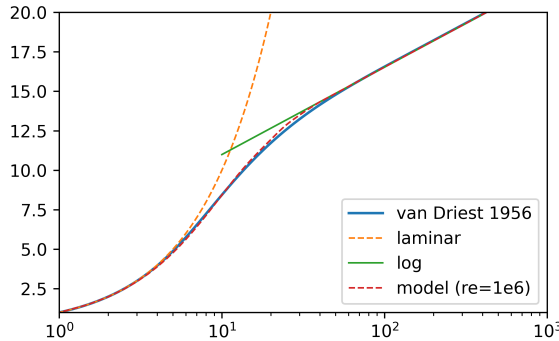


**Fig. 11** Near-wall velocity profile according to the van-Driest scaling (blue, solid) in comparison with the present model (red, dashed), the viscous law of the wall (orange dashed), and the logarithmic law (green, solid)

554 where large scales leave their signatures in vicinity of the surface. It is important  
 555 to note here that, while  $V$  is a first-order statistic from a statistical perspective,  
 556 the spanwise velocity is a higher-order correction term from the perspective of sim-  
 557 ilarity theory and from the viewpoint of the channel-flow analogy that is routinely  
 558 employed in the surface layer. Further, this is consistent with the scaling for the  
 559 velocity hodograph found in Eq. (10) where the friction velocity also drops out.

560 In the surface layer, there is not only a mixed scaling—as we had already iden-  
 561 tified in the viscous layer—but we cannot find a universal function onto which the  
 562 profiles of spanwise velocity collapse. This additional degree of freedom reflects  
 563 the inner–outer matching problem for the spanwise velocity. Rather than giving  
 564 a universal profile for this region, we resort here to a parametric description of  
 565 the problem in terms of the function  $f_{V,\log}$  determined by the parameters  $a_{\log}$ ,  
 566  $b_{\log}$ ,  $c_{\log}$  which can be estimated based on the above scaling considerations for  
 567 any Reynolds number. We note that, once the parameter  $a_{\log}$  is known, the pa-  
 568 rameters  $b_{\log}$  and  $c_{\log}$  can be estimated solely based on  $f_{V,\text{visc}}$ , i.e. using the value  
 569  $v_{10}$  and  $d_{10}$  found for the viscous region of the flow. For the range of Reynolds  
 570 number relevant to geophysical problems ( $10^4 \lesssim \text{Re}_D \lesssim 10^6$ ), the variation of  $c_{\log}$   
 571 is, however, rather small.

## 572 5.2 Comparison with other theories

573 An alternative approach that considers viscous effects close to the surface is the  
 574 van-Driest scaling (Van Driest 1956), where an exponential damping of Prandtl's  
 575 mixing length is considered near the wall to yield

$$\frac{\partial u^+}{\partial z^+} = \frac{2}{1 + \sqrt{1 + (2\kappa z^+)^2 (1 - \exp[-z^+])}}; \quad (16)$$

576 the spanwise component is zero as no rotational effects are considered. Compar-  
 577 ing our proposed formulation for the stream-wise velocity in the inner layer to  
 578 Van Driest's formulation yields later convergence of the velocity onto the loga-  
 579 rithmic profile while, over all, it serves as an excellent model of the streamwise

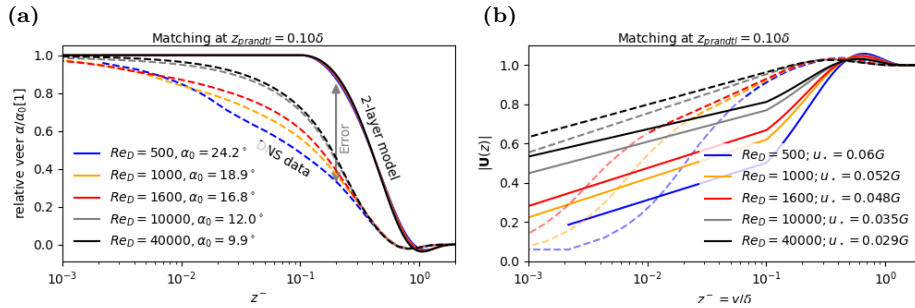


**Fig. 12** Comparison of the DNS data (dashed lines) with the two-layer model proposed by Etling (solid lines) for different Reynolds number. Left panel shows the relative wind veer, right panel shows the velocity magnitude. The Etling model is calibrated by the surface veer from the DNS and the roughness parameter is chosen according to the correction factor  $\exp \kappa A$  such that the total veer and velocity magnitude agree. Profiles in the buffer layer, defined here as  $z^+ < 30$  are shown as opaque dashed lines as the two-layer model does not consider viscous effects.

velocity component (Fig. 11): Notable deviations (on the order of few percent) only occur in the region  $10 < z^+ < 30$ , where the velocity transitions from the linear to the logarithmic profile.

For the higher layers of the ABL, the Ekman spiral is the simplest model available. When employed across the entirety of the ABL, the spiral of a turbulent Ekman layer is flattened with respect to Ekman's laminar solution, which corresponds to a reduction of the veering angle both at the surface and throughout the ABL. We, however, find that a modified version of the Ekman spiral explicitly taking into account the surface boundary condition, is a consistent model and yields excellent agreement with the velocity profiles from DNS (Sec. 4.2).

A two-layer model consolidating both the logarithmic and Ekman layer can be obtained following the arguments by Etling (2008), cf. Emeis (2018). Given a surface veering and a matching height (extent of the logarithmic layer), a formulation for the velocity profile across both the logarithmic and the outer layer is obtained. A comparison using the surface veering based on our model and a matching height of  $z_{\text{prandtl}} = 0.05\delta$ , which gives better results than the matching height of  $0.1\delta$  suggested by Etling (2008), is shown in Fig. 12. The overall shape of velocity magnitude is matched apart from the viscous and buffer layer (cf. Fig. 12b) that is neglected by the two-layer model. However, quantitative departures on the order of 10% occur across the inner layer: it turns out that the non-rotating profile, of the two-layer model in the logarithmic region yields too low overall velocity as the spanwise component contributes to the velocity across the inner layer. Deviations also occur with respect to wind direction; despite the rather low matching height, a substantial fraction of the rotation occurs within the lower part of the ABL and about 20% of the wind veer is not captured by the two-layer model. As the overall veer is given, the non-captured veer close to the surface is then compensated across the logarithmic layer. In the upper part of the boundary layer, both profiles match well.

The interpretation of flux and gradient profiles in terms of the K-theory (cf. Sec. 3, Fig. 2) suggests a certain universality in the inner layer, while a global collapse, i.e. across the boundary layer, is not obtained. While the K-Profiles con-

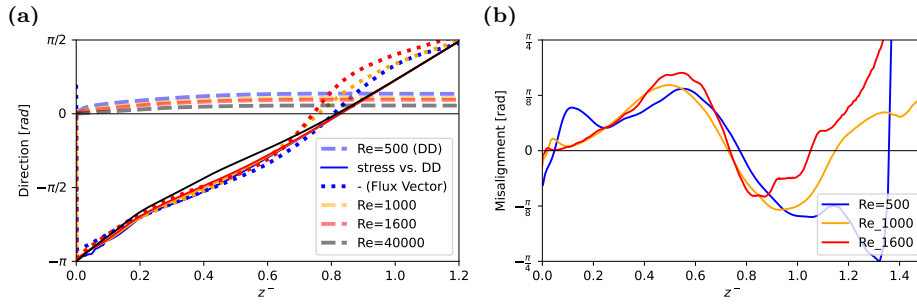


**Fig. 13** Panel (a) shows the wind direction (DD) as thick dashed lines and the direction of stress relative to DD as thin solid lines, both according to our profile model. The direction of the negative flux vector ( $u'w'$ ,  $v'w'$ ) based on DNS data is shown as a dotted line. In panel (b), we plot the misalignment, i.e. the angle, between the flux vector and the shear vector, where the shear vector is defined accordingly as  $(\partial_z U, \partial_z V)$ .

cern the total stress, a consistent formulation of the turning would also require its partitioning to the individual components, i.e. the orientation of the stress vector ( $u'w'$ ,  $v'w'$ ) in the horizontal plane. If K-theory shall be used, this stress vector needs to be anti-parallel to the corresponding stress vector ( $\partial_z U, \partial_z V$ ). Fig. 13 shows the direction of the velocity, gradient and stress vectors across the boundary layer. It turns out that the negative stress vector with respect to the wind direction and the flux vectors (absolute) have an approximately similar direction. It appears that both rotate by about  $270^\circ$  ( $3\pi/2$ ) across the boundary layer. Apart from the lower part of the Ekman layer ( $0.2 < z^- < 0.7$ ), where there is a slight dependence on  $Re$ , the direction of stress appears to be universal, which is a consequence of the Ekman profile introduced in Sec. 4.2. However, this implies a misalignment between the flux and the stress on the order of the wind turning, and indeed Fig. 13b shows a misalignment up to  $\pi/8$ . This is in accordance with the expectation by (Townsend 1976, Chap. 7.18) and prevents the transfer of energy from the mean flow to turbulence at these heights, thus preventing a boundary-layer growth. While the behavior in the inner layer seems to depend on  $Re$ , there emerges universality in the misalignment across the outer layer, suggesting that a consideration of misalignment in the context of K-theory is possible when developing formulations for higher-order quantities.

## 6 Conclusions

We investigate the wind veer and fundamental scaling properties of the velocity profiles in Ekman flow. Based on scaling considerations and direct numerical simulation spanning a decade in external separation from  $Re_A = 1.25 \times 10^5$  to  $Re_A = 1.28 \times 10^6$ , we derive a universal formulation for the both horizontal components of the velocity profile in a stationary, smooth Ekman layer. This formulation is consistent with the DNS data and also yields reasonable results at geophysical scale separation; the logarithmic law of the mean velocity is recovered with the well-known limits and deviations towards the surface and Ekman layer. The classic formulation of the Ekman layer, employing the surface boundary condition, is replaced by a modified solution that can be obtained by Ekman's system of govern-

ing equations, but using different boundary conditions that are more appropriate of the actual situation encountered in the planetary boundary layer. The three parameters that characterize this boundary condition are estimated based on DNS data.

To quantify the spanwise velocity component consistently across the boundary layer, we derive a universal scaling of the spanwise velocity component in a shear-aligned reference frame. For the *inner layer*, we find the mixed scaling

$$V^{\alpha*}/G = \frac{1}{\delta^+} f(z^+) \quad (17)$$

that is, the spanwise velocity normalized by the outer velocity scale is a universal function of the inner height and Friction Reynolds number  $Re_\tau = \delta^+$ . This scaling is derived here based on scaling considerations, and it is in excellent agreement with the DNS data available. In the outer layer, the spanwise velocity follows outer scaling, consistently with the Ekman model discussed above (Sec. 4.2).

Our results suggest that there is no lower limit of the turning. Hence—despite its very large scale separation / huge Reynolds number—the ABL is not in the ‘limit’ of high Reynolds number from the perspective of wind veer, but always in a regime where changes in Re impact on the vertical partitioning of rotation.

## 657 A Laminar Ekman solution with consideration of inner layer

658 The following Ekman system is obtained by averaging the Navier–Stokes equations horizontally  
659 and over time and neglecting the turbulent transport terms (turbulence can then be considered  
660 via the eddy-viscosity concept through variations in the viscosity  $\nu$ ):

$$\begin{pmatrix} \partial_t U \\ \partial_t V \end{pmatrix} = \begin{pmatrix} fV & + \nu \partial_z^2 U \\ -f(U - G) & + \nu \partial_z^2 V \end{pmatrix} \quad (18a)$$

$$\Rightarrow \partial_t(U + iV) = f(V - i(U - G)) + \nu \partial_z^2(U + iV) \quad (18b)$$

661 In stationary conditions, this system is solved by

$$\hat{u}(z) = U_\infty + e^{-\gamma z} [A \cos \gamma z + B \sin \gamma z] \quad (18c)$$

$$\hat{v}(z) = V_\infty + e^{-\gamma z} [-A \sin \gamma z + B \cos \gamma z] \quad (18d)$$

662 where the constants  $U_\infty$ ,  $V_\infty$  set the top boundary condition and  $A$  and  $B$  set the bottom  
663 boundary condition. The most common boundary condition for a surface Ekman layer is  $A =$   
664  $U_\infty = G$ ,  $B = 0$ , and  $V_\infty = 0$ . The lower boundary condition, however, neglects the existence  
665 of the surface layer, and it appears reasonable to define  $A = cG$  where  $c < 1$  is a constant  
666 that **incorporates** the increased shear in the surface layer. Given a ‘matching height’  $z_{match}$  and  
667 normalized matching height  $\xi = \gamma z_{match}$  in the upper part of the inner layer, we can match  
668 the Ekman profile to the inner layer by letting

$$\begin{aligned} u(z_{match}) &\equiv u_{match} = U_\infty + e^{-\xi} [A \cos \xi + B \sin \xi] \\ v(z_{match}) &\equiv v_{match} = V_\infty + e^{-\xi} [-A \sin \xi + B \cos \xi] \end{aligned} \quad (19a)$$

$$\Rightarrow \begin{pmatrix} u_{match} - U_\infty \\ v_{match} - V_\infty \end{pmatrix} = e^{-\xi} \begin{pmatrix} A \\ B \end{pmatrix} \begin{pmatrix} \cos \xi & + \sin \xi \\ -\sin \xi & + \cos \xi \end{pmatrix} \quad (19b)$$

$$(19c)$$

670 Matching the profile at  $\xi = 0$ , one obtains  $A = \Delta u_{match}$  and  $B = -\Delta w_{match}$ ; and when the  
671 direction  $Ox$  is aligned with the geostrophic wind, we obtain the textbook-case  $A = |\mathbf{G}|$  and  
672  $B = 0$ .

673 Otherwise, choosing  $B \neq 0$  allows to introduce a phase shift of the Ekman rotation with  
674 respect to the decay of the wind spiral. However, in our context, the thickness and position of  
675 the spiral can already be controlled by the eddy viscosity and an offset in  $\xi$ , here we let  $B = 0$ .

676 **B Matching the spanwise velocity profiles in the inner layer**

677 The spanwise profile in vicinity of the surface is given by  $V/G = f_{V,\text{visc}}\delta^+$  with

$$f_{V,\text{visc}} = v_{\text{ref}} \left( \omega_v z^+ - 1 + e^{-\omega_v z^+} \right) \quad (20\text{a})$$

$$f_{V,\log} = a_{\log} + b_{\log} \log z^+ + c_{\log} z^+ \quad (20\text{b})$$

678 Matching the profiles and gradient  $z_0 = 10^+$  and the value at  $z_1 = 0.3\delta^+$  yields

$$v_{\text{ref}} (\omega_v z_0 + e^{-\omega_v z_0}) = v_0 = a_{\log} + b_{\log} \log z_0 + c_{\log} z_0 \quad (21\text{a})$$

$$v_1 = a_{\log} + b_{\log} \log z_1 + c_{\log} z_1 \quad (21\text{b})$$

$$v_{\text{ref}} \omega_z (1 - e^{-\omega_z z_0}) = d_0 = \frac{b_{\log}}{z_{10}} + c_{\log} \quad (21\text{c})$$

679 The gradient condition implies  $b_{\log} = (d_0 - c_{\log})z_0$ , and yields

$$v_0 - z_0 d_0 \log z_0 = a_{\log} + c_{\log} (z_0 - z_0 \log z_0) \quad (22\text{a})$$

$$v_1 - z_0 d_0 \log z_1 = a_{\log} + c_{\log} (z_1 - z_0 \log z_0) \quad (22\text{b})$$

$$\Rightarrow c_{\log} = \frac{\Delta v - z_0 d_0 \log z_1 / z_0}{\Delta z} \quad (22\text{c})$$

680 with  $\Delta z = z_1 - z_0$  and  $\Delta v = v_1 - v_0$ . Then, the coefficient  $a_{\log}$  is estimated as

$$a_{\log} = v_0 - z_0 d_0 \log z_0 - \frac{\Delta v - z_0 d_0 \log z_1 / z_0}{\Delta z} [z_0 - z_0 \log z_0]. \quad (22\text{d})$$

681 We note that  $\log(z_1/z_0)/(z_1 - z_0) \rightarrow 0$  for large  $z_1$ , and as  $z_1 = 0.3\delta^+$ , this implies that the  
682 second term in  $c_{\log}$  only plays a role at low and intermediate Re. Then,  $a_{\log}$  can be estimated  
683 as

$$a_{\log} \simeq v_0 - z_0 \left[ d_0 \log z_0 - \frac{\Delta v}{\Delta z} (1 - \log z_0) \right] \quad (22\text{e})$$

684 for large Re.

685 **Acknowledgements** This study is funded by the European Commission's 7<sup>th</sup> Framework Pro-  
686 gramme through the ERC 2019 Starting Grant *trainABL* (ID 851374). Simulations were carried  
687 out on the German supercomputing systems **hawk** at Höchstleistungsrechenzentrum Stuttgart  
688 (Bundesprojekt 44187) and **juwels** at Gauss Centre for supercomputing, Forschungszentrum  
689 Jülich (Projects **hku24** and **stadit**). We extend our thanks to Sally Issa for valuable feedback  
690 on the manuscript.

691 **Declarations**

692 **Author Contributions** CA conceived the study, acquired funding, performed the simulation,  
693 analysed and plotted the data for this work. CA and HW interpreted the data and compiled  
694 the manuscript.

695 **Funding** CA is funded by ERC Starting Grant *trainABL* (ID 851374). Open Access funding  
696 for this publication through the DEAL agreement.

697 **Data Availability** The data is available in long-term repositories and indexed by DOIs as  
698 cited in the list of references. Further analysis tools and processed data can be made available  
699 upon direct request.

700 **Conflict of Interest** The Authors declare no competing interest.

701 **Open Access** This article is licensed under a Creative Commons Attribution 4.0 International  
702 License, which permits use, sharing, adaptation, distribution and reproduction in any medium  
703 or format, as long as you give appropriate credit to the original author(s) and the source,  
704 provide a link to the Creative Commons licence, and indicate if changes were made. To view  
705 a copy of this licence, visit <https://creativecommons.org/licenses/by/4.0/>.

706 **References**

- Ansorge C (2019) Scale Dependence of Atmosphere–Surface Coupling Through Similarity Theory. *Boundary-Layer Meteorol* 170(1):1–27, DOI 10.1007/s10546-018-0386-y
- Ansorge C (2024a) Direct numerical simulation of turbulent Ekman flow (Re=500): DOI 10.17169/refubium-42505. DOI 10.17169/refubium-42505
- Ansorge C (2024b) Direct numerical simulation of turbulent Ekman flow (Re=1000): DOI 10.17169/refubium-42507. DOI 10.17169/refubium-42507
- Ansorge C (2024c) Direct numerical simulation of turbulent Ekman flow (Re=1300): DOI 10.17169/refubium-42508. DOI 10.17169/refubium-42508
- Ansorge C (2024d) Direct numerical simulation of turbulent Ekman flow (Re=1600): DOI 10.17169/refubium-42509. DOI 10.17169/refubium-42509
- Ansorge C, Mellado JP (2014) Global Intermittency and Collapsing Turbulence in the Stratified Planetary Boundary Layer. *Boundary-Layer Meteorol* 153(1):89–116, DOI 10.1007/s10546-014-9941-3
- Ansorge C, Mellado JP (2016) Analyses of external and global intermittency in the logarithmic layer of Ekman flow. *J Fluid Mech* 805:611–635, DOI 10.1017/jfm.2016.534
- Baars WJ, Marusic I (2020) Data-driven decomposition of the streamwise turbulence kinetic energy in boundary layers. Part 2. Integrated energy and. *J Fluid Mech* 882:A26, DOI 10.1017/jfm.2019.835
- Barenblatt GI (1993) Scaling laws for fully developed turbulent shear flows. Part 1. Basic hypotheses and analysis. *J Fluid Mech* 248:513–520, DOI 10.1017/S0022112093000874
- Barenblatt GI, Goldenfeld N (1995) Does fully developed turbulence exist? Reynolds number independence versus asymptotic covariance. *Phys Fluids* 7(12):3078–3082, DOI 10/bw2sq5
- Blackadar AK, Tennekes H (1968) Asymptotic Similarity in Neutral Barotropic Planetary Boundary Layers. *Journal of the Atmospheric Sciences* 25:1015–1020, DOI 10.1175/1520-0469(1968)025(1015:ASINBP)2.0.CO;2
- Brown AR, Beljaars ACM, Hersbach H, Hollingsworth A, Miller M, Vasiljevic D (2005) Wind turning across the marine atmospheric boundary layer. *Quarterly Journal of the Royal Meteorological Society* 131(607):1233–1250, DOI 10/dw2bxz
- Calaf M, Meneveau C, Meyers J (2010) Large eddy simulation study of fully developed wind-turbine array boundary layers. *Phys Fluids* 22(1):015,110, DOI 10/b7gc6v
- Coleman GN, Ferziger JH, Spalart PR (1992) Direct Simulation of the Stably Stratified Turbulent Ekman Layer. *Journal of Fluid Mechanics* 244:677–712, DOI 10.1017/S0022112092003264
- da Silva CB, Hunt JC, Eames I, Westerweel J (2014) Interfacial Layers Between Regions of Different Turbulence Intensity. *Annu Rev Fluid Mech* 46(1):567–590, DOI 10.1146/annurev-fluid-010313-141357
- Dimotakis PE (2005) TURBULENT MIXING. *Annual Review of Fluid Mechanics* 37(1):329–356, DOI 10.1146/annurev.fluid.36.050802.122015
- Ekman VW (1905) On the influence of the earth's rotation on ocean currents. *Ark Mat Astron Fys*, Vol 2 (1905), pp 1-53 2:1–53
- Ellison TH (1955) The Ekman spiral. *Q J Roy Met Soc* 81(350):637–638, DOI 10.1002/qj.49708135025
- Emeis S (2018) Wind Energy Meteorology, 2nd edn. *Atmospheric Physics for Wind Power Generation*, Springer, Heidelberg
- Emeis S, Baumann-Stanzer K, Piringer M, Kallistratova M, Kouznetsov R, Yushkov V (2007) Wind and turbulence in the urban boundary layer analysis from acoustic remote sensing data and fit to analytical relations. *metz* 16(4):393–406, DOI 10.1127/0941-2948/2007/0217
- Esau I (2004) Simulation of Ekman Boundary Layers by Large Eddy Model with Dynamic Mixed Subfilter Closure. *Environmental Fluid Mechanics* 4(3):273–303, DOI 10/b8f3kh
- Eting D (2002) Theoretische Meteorologie, 2nd edn. Eine Einführung, Springer-Verlag, Berlin, Heidelberg
- Eting D (2008) Theoretische Meteorologie: eine Einführung, 3rd edn. Springer, Berlin Heidelberg
- Foken T (2002) Some aspects of the viscous sublayer. *metz* 11(4):267–272, DOI 10.1127/0941-2948/2002/0011-0267
- Foken Th, Kitajgorodskij SA, Kuznecov OA (1978) On the dynamics of the molecular temperature boundary layer above the sea. *Boundary-Layer Meteorol* 15(3):289–300, DOI 10.1007/BF02652602

- 765 Ghannam K, Bou-Zeid E (2021) Baroclinicity and directional shear explain departures from  
766 the logarithmic wind profile. *Quarterly Journal of the Royal Meteorological Society* 147:434–  
767 464, DOI 10/gnj6z2
- 768 Gryning SE, Batchvarova E, Brümmer B, Jørgensen H, Larsen S (2007) On the extension of the  
769 wind profile over homogeneous terrain beyond the surface boundary layer. *Boundary-Layer  
770 Meteorol* 124(2):251–268, DOI 10.1007/s10546-007-9166-9
- 771 Höglström U (1988) Non-dimensional wind and temperature profiles in the atmospheric surface  
772 layer: A re-evaluation. *Boundary-Layer Meteorology* 42:55–78, DOI 10.1007/BF00119875
- 773 Höglström U (1996) Review of some basic characteristics of the atmospheric surface layer.  
774 *Boundary-Layer Meteorology* 78(3-4):215–246, DOI 10.1007/BF00120937
- 775 Jacobs AF, Van Boxel JH (1988) Changes of the displacement height and roughness length  
776 of maize during a growing season. *Agricultural Forest Meteorol* 42(1):53–62, DOI 10.1016/  
777 0168-1923(88)90066-4
- 778 Jiang Q, Wang S, Sullivan P (2018) Large-Eddy Simulation Study of Log Laws in a Neutral  
779 Ekman Boundary Layer. *Journal of the Atmospheric Sciences* 75(6):1873–1889, DOI 10.  
780 1175/JAS-D-17-0153.1
- 781 Jiménez J (2012) Cascades in Wall-Bounded Turbulence. *Ann Rev Fluid Mech* 44(Volume 44,  
782 2012):27–45, DOI 10.1146/annurev-fluid-120710-101039
- 783 Kelly M, Gryning SE (2010) Long-Term Mean Wind Profiles Based on Similarity Theory.  
784 *Boundary-Layer Meteorol* 136(3):377–390, DOI 10.1007/s10546-010-9509-9
- 785 Kelly M, Troen I (2016) Probabilistic stability and ‘tall’ wind profiles: Theory and method for  
786 use in wind resource assessment. *Wind Energy* 19(2):227–241, DOI 10.1002/we.1829
- 787 Klein M, Maier RE, Schmidt H (2021) Stochastic modeling of transient neutral and stably-  
788 stratified Ekman boundary layers. *P A M M* 21(1):e202100,146, DOI 10.1002/pamm.  
789 202100146
- 790 Li Q, Gentine P, Mellado JP, McColl KA (2018) Implications of Nonlocal Transport and  
791 Conditionally Averaged Statistics on Monin–Obukhov Similarity Theory and Townsend’s  
792 Attached Eddy Hypothesis. *J Atmos Sci* 75(10):3403–3431, DOI 10.1175/JAS-D-17-0301.1
- 793 Lindvall J, Svensson G (2019) Wind turning in the atmospheric boundary layer over land. *Q  
794 J Roy Met Soc* 145(724):3074–3088, DOI 10.1002/qj.3605
- 795 Mellado J, Ansorge C (2012) Factorization of the Fourier transform of the pressure-Poisson  
796 equation using finite differences in colocated grids. *Z angew Math Mech* 92(5):380–392,  
797 DOI 10.1002/zamm.201100078
- 798 Mellado JP, van Heerwaarden CC, Garcia JR (2016) Near-Surface Effects of Free Atmosphere  
799 Stratification in Free Convection. *Boundary-Layer Meteorol* 159(1):69–95, DOI 10.1007/  
800 s10546-015-0105-x
- 801 Mirocha JD, Churchfield MJ, Muñoz-Esparza D, Rai RK, Feng Y, Kosović B, Haupt SE,  
802 Brown B, Ennis BL, Draxl C, Sanz Rodrigo J, Shaw WJ, Berg LK, Moriarty PJ, Linn RR,  
803 Kotamarthi VR, Balakrishnan R, Cline JW, Robinson MC, Ananthan S (2018) Large-eddy  
804 simulation sensitivities to variations of configuration and forcing parameters in canonical  
805 boundary-layer flows for wind energy applications. *Wind Energy Science* 3(2):589–613, DOI  
806 10/gn3nh4
- 807 Moin P, Mahesh K (1998) Direct numerical simulation: A tool in turbulence research. *Annual  
808 Review of Fluid Mechanics* 30:539–578, DOI 10.1146/annurev.fluid.30.1.539
- 809 Momen M, Bou-Zeid E (2016) Large-Eddy Simulations and Damped-Oscillator Models of the  
810 Unsteady Ekman Boundary Layer\*. *Journal of the Atmospheric Sciences* 73(1):25–40, DOI  
811 10.1175/JAS-D-15-0038.1
- 812 Momen M, Bou-Zeid E, Parlange MB, Giometto M (2018) Modulation of Mean Wind and  
813 Turbulence in the Atmospheric Boundary Layer by Baroclinicity. *Journal of the Atmospheric  
814 Sciences* 75(11):3797–3821, DOI 10/gfmn67
- 815 Monin AS (1970) The Atmospheric Boundary Layer. *Annual Review of Fluid Mechanics* 2:225–  
816 250, DOI 10.1146/annurev.fl.02.010170.001301
- 817 Monin AS, Yaglom AM (1975) Statistical Fluid Mechanics, Vol. II, Dover Publications on  
818 Physics, vol II. Dover Publications, Inc., Mineola
- 819 Optis M, Monahan A, Bosveld FC (2014) Moving Beyond Monin-Obukhov Similarity The-  
820 ory in Modelling Wind-Speed Profiles in the Lower Atmospheric Boundary Layer un-  
821 der Stable Stratification. *Boundary-Layer Meteorology* 153(3):497–514, DOI 10.1007/  
822 s10546-014-9953-z
- 823 Rossby CG, Montgomery RB (1935) The layer of frictional influence in wind and ocean cur-  
824 rents. *Papers in Physical Oceanography and Meteorology* III(3):1–101

- 825 Sakagami Y, Haas R, Passos JC (2020) Generalized Non-dimensional Wind and Temperature  
826 Gradients in the Surface Layer. *Boundary-Layer Meteorol* 175(3):441–451, DOI 10.1007/  
827 s10546-020-00510-3
- 828 Spalart PR (1989) Theoretical and numerical study of a three-dimensional turbulent boundary  
829 layer. *J Fluid Mech* 205(-1):319, DOI 10.1017/S0022112089002053
- 830 Spalart PR, Coleman GN, Johnstone R (2008) Direct numerical simulation of the Ekman layer:  
831 A step in Reynolds number, and cautious support for a log law with a shifted origin. *Phys  
832 Fluids* 20(10):101,507, DOI 10.1063/1.3005858
- 833 Spalart PR, Coleman GN, Johnstone R (2009) Retraction: “Direct numerical simulation of the  
834 Ekman layer: A step in Reynolds number, and cautious support for a log law with a shifted  
835 origin” [Phys. Fluids 20, 101507 (2008)]. *Phys Fluids* 21(10):109,901, DOI 10.1063/1.3247176
- 836 Stoll R, Gibbs JA, Salesky ST, Anderson W, Calaf M (2020) Large-Eddy Simulation of the At-  
837mospheric Boundary Layer. *Boundary-Layer Meteorol* 177(2-3):541–581, DOI 10/gmbmzw
- 838 Svensson G, Holtslag AAM (2009) Analysis of Model Results for the Turning of the Wind  
839 and Related Momentum Fluxes in the Stable Boundary Layer. *Boundary-Layer Meteorol*  
840 132(2):261–277, DOI 10/bwknmt
- 841 Tennekes H (1973) A Model for the Dynamics of the Inversion Above a Convective Boundary  
842 Layer. *Journal of the Atmospheric Sciences*
- 843 Townsend AA (1976) The Structure of Turbulent Shear Flow, 2nd edn. Cambridge University  
844 Press
- 845 Van Driest ER (1956) On Turbulent Flow Near a Wall. *Journal of the Aeronautical Sciences*  
846 23(11):1007–1011, DOI 10.2514/8.3713
- 847 Zikanov O, Slinn DN, Dhanak MR (2003) Large-eddy simulations of the wind-induced turbu-  
848 lent Ekman layer. *J Fluid Mech* 495:343–368, DOI 10/ccbpbw